Magnetospheric Multiscale Observation of Kinetic Signatures in the Alfvén Vortex

Tieyan Wang[1] , Olga Alexandrova[2], Denise Perrone[3] , Malcolm Dunlop[1,4], Xiangcheng Dong[4], Robert Bingham[1],
Yu. V. Khotyaintsev[5] , C. T. Russell[6] , B. L. Giles[7], R. B. Torbert[8], R. E. Ergun[9], and J. L. Burch[10]

[1] RAL Space, Rutherford Appleton Laboratory, Harwell Oxford, Didcot OX11 0QX, UK
[2] LESIA, Observatoire de Paris, Université PSL, CNRS, Sorbonne Université, Univ. Paris Diderot,
Sorbonne Paris Cité, 5 place Jules Janssen, 92195 Meudon, France
[3] Department of Physics, Imperial College London, London SW7 2AZ, UK
[4] School of Space and Environment, Beihang University, Beijing 100191, People's Republic of China
[5] Swedish Institute of Space Physics, Uppsala, Sweden
[6] Institute of Geophysics and Planetary Physics, University of California, Los Angeles, CA, USA
[7] NASA Goddard Space Flight Center, Greenbelt, MD 20771, USA
[8] University of New Hampshire, Durham, NH, USA
[9] Laboratory of Atmospheric and Space Physics, University of Colorado, Boulder, CO 80303, USA
[10] Southwest Research Institute San Antonio, San Antonio, TX 78238, USA

Abstract

Alfvén vortex is a multiscale nonlinear structure that contributes to the intermittency of turbulence. Despite previous explorations mostly on the spatial properties of the Alfvén vortex (i.e., scale, orientation, and motion), the plasma characteristics within the Alfvén vortex are unknown. Moreover, the connection between the plasma energization and the Alfvén vortex still remains unclear. Based on high-resolution in situ measurements from the Magnetospheric Multiscale mission, we report for the first time distinctive plasma features within an Alfvén vortex. This Alfvén vortex is identified as being a 2D ($k_\perp \gg k_\parallel$) quasi-monopole with a radius of 10 proton gyroscales. Its magnetic fluctuations $\delta B_\perp$ are anti-correlated with velocity fluctuations $\delta V_\perp$, thus the parallel current density $j_\parallel$ and flow vorticity $\omega_\parallel$ are anti-aligned. In different part of the vortex (i.e., edge, middle, center), the ion and electron temperatures are found to be quite different and they behave in the reverse trend: the ion temperature variations are correlated with $j_\parallel$, while the electron temperature variations are correlated with $\omega_\parallel$. Furthermore, the temperature anisotropies, together with the non-Maxwellian kinetic effects, exhibit strong enhancement at peaks of $|\omega_\parallel|(|j_\parallel|)$ within the vortex. Comparison between observations and numerical/theoretical results are made. In addition, the energy-conversion channels and the compressibility associated with the Alfvén vortex are discussed. These results may help to understand the link between coherent vortex structures and the kinetic processes, which determines how turbulence energy dissipates in the weakly collisional space plasmas.

Key words: plasmas – turbulence

1. Introduction

Turbulence typically manifests itself as disordered, self-organized structures across different scales, resulting from nonlinear interactions of various physical properties with many degrees of freedom. Astrophysical plasmas such as the interstellar medium and stellar atmosphere are found to exist in a turbulent state, and the solar-terrestrial environment is no exception (Tu & Marsch 1995; Chang 1999; Zimbardo et al. 2010). Understanding how the magnetized plasma turbulence works is challenging as it involves complex interactions between the electromagnetic fields and particles, leading to a state far from thermal equilibrium. Two fundamental properties have been found to explain how the turbulence energy redistributes (usually referred to as "cascade") from large system scales to small kinetic scales. One is the power-law scaling of the turbulence energy spectrum at the so-called inertial range, where phenomenological approaches (e.g., Frisch 1995; Biskamp 2003) are used to describe the self-similar (scale-invariant) fluctuations. However, the fully developed turbulence never displays pure scale invariance, instead it is characterized by bursty fluctuations emerging spontaneously. This property is referred to as intermittency, usually recognized by an increase of non-Gaussianity for the statistics of the fluctuations toward smaller scales (i.e., the scale-dependent sharpening of the central peak and the heavy

tail of the probability distribution function (PDF) in Sorriso-Valvo et al. (2001). It is conjectured that, as the turbulence cascade proceeds, the inhomogeneous transfer of energy toward small scales will lead to an uneven concentration of energy in limited volumes, thereby forming a series of patchy, phase-correlated structures localized in space (Frisch 1995; Alexandrova et al. 2013; Chen 2016). Although the physical mechanisms for the generation of coherent structures are still unclear, the intermittent events are believed to be crucial for the localized energy transfer and dissipation process.

Intermittency in hydrodynamics is depicted in high-amplitude tube-like vortex filaments (She et al. 1990), where the vorticity is most likely aligned with the intermediate eigenvector of the strain rate (Ashurst et al. 1987). These filament objects have two characteristic lengths. The larger one is comparable to the system size, at which the energy is injected. The smaller one is close to the Kolmogorov dissipation length, where the molecular dissipation kicks in. Due to the inherently complex nature of the space plasma, the intermittent structures in this system exhibit more characteristic scales (e.g., magneto-fluid scale, and ion and electron gyroscales) and topologies than that in the neutral fluid. Among various textures in plasma turbulence, current sheets, vortices, magnetic holes, solitons, and shocks have been commonly observed (Veltri & Mangeney 1999; Alexandrova et al. 2006; Greco et al. 2016; Lion et al. 2016;

Perrone et al. 2016, 2017; Roberts et al. 2016; Huang et al. 2017; Zhang et al. 2018). Structures with strong gradients and relatively simple geometries (i.e., current sheet, rotational/ tangential discontinuities) can be easily identified based on partial variance increment techniques (Greco et al. 2008). Subsequently, evidence for turbulence dissipation, plasma heating, and temperature anisotropy have been found near the current sheet/discontinuities in observations and simulations (Retinò et al. 2007; Parashar et al. 2009; Osman et al. 2012a, 2012b; Servidio et al. 2012; Wan et al. 2012; Karimabadi et al. 2013; Wang et al. 2013; Wu et al. 2013; Perrone et al. 2014; Chasapis et al. 2015; Zhang et al. 2015; Valentini et al. 2016; Yordanova et al. 2016; Vörös et al. 2017; Camporeale et al. 2018). In particular, the location of plasma heating is reported to be in better agreement with places of vorticity than current density (i.e., simulation in Franci et al. 2016; Parashar & Matthaeus 2016), indicating that the velocity gradient is as important as, if not more crucial than, the magnetic gradient.

In analogy to the hydrodynamic case, the nonlinear coherent vortex structure also plays an important role in plasma dynamics and transport processes (Hasegawa & Mima 1978; Shukla et al. 1985; Petviashvili & Pokhotelov 1992; Horton & Hasegawa 1994). These vortices tend to have a long lifetime and are widely observed in space, laboratory, and numerical simulation of plasma (Chmyrev et al. 1988; Burlaga 1990; Volwerk et al. 1996; Stasiewicz et al. 2000; Sundkvist et al. 2005; Alexandrova et al. 2006; Alexandrova 2008; Alexandrova & Saur 2008; Vianello et al. 2010; Servidio et al. 2015). An essential subset of these plasma vortices is known as Alfvén vortices, which can be viewed as the cylindrical analog of the nonlinear Alfvén wave (Petviashvili & Pokhotelov 1992). The Alfvén vortices have an axis that is nearly parallel to the unperturbed magnetic field, along which the shape is generally invariant. Thus, these vortices are quasi-2D structures. The associated perpendicular magnetic fluctuations are linearly related with the perpendicular velocity fluctuations, but their relative amplitudes are not obligatorily equal (as is the case in an Alfvén wave): $\delta V_\perp / V_A = \xi \delta B_\perp / B_0$, where ξ is not necessarily equal to 1. In addition, Alfvén vortices do not propagate along B_0 in the plasma frame, and they hardly propagate in the perpendicular plane when the axis of the vortex is inclined with respect to B_0 that are in contrast with Alfvén wave (Wang et al. 2012). After first being reported in the Earth's magnetosheath (Alexandrova et al. 2006; Alexandrova 2008), multiscale quasi-bidimensional Alfvén vortices (with $k_\perp \gg k_\parallel$) have been identified in numerous space environments: in slow solar wind (Perrone et al. 2016; Roberts et al. 2016), in fast solar wind (Lion et al. 2016; Perrone et al. 2017), and in Saturn's magnetosheath (Alexandrova & Saur 2008). It seems that the intermittent structures in fast solar wind are dominated by Alfvén vortices (Perrone et al. 2017), which agrees with the 2D MHD turbulence model (Zank et al. 2017).

Due to the limited temporal resolution of the plasma instrument on previous missions (i.e., the Cluster mission in Escoubet et al. 2001), most of the Alfvén vortices have been identified solely on the basis of magnetic field measurement (Perrone et al. 2016, 2017; Roberts et al. 2016). An attempt to estimate velocity fluctuations δV using the electric and magnetic field data was done in Alexandrova et al. (2006). It was shown that indeed magnetic and velocity fluctuations are well aligned as expected for an Alfvén vortex. This result,

however, needs to be confirmed by the direct measurements of the flow properties. Moreover, the knowledge of plasma characteristics, especially the velocity distribution functions (VDFs) accompanied with Alfvén vortices, still remains blank. Although some results of electrons are discussed in Perrone et al. (2017), the 4 s resolution for the particle data was far from enough as compared to the vortex timescale. This led us to wonder: what are the detailed ion and electron behaviors within the Alfvén vortices? Is there any connection between Alfvén vortices and plasma kinetic effects? Thanks to the Magnetospheric Multiscale (MMS) mission (Burch et al. 2016), four closely separated probes measure the turbulent magnetosheath region and provide high temporal resolution particle data during its burst mode (150 ms for ions and 30 ms for electrons). This allows us to overcome the major observational obstacles and resolve the sub-ion scales features of the vortex. In this Letter, for the first time we (i) verify the $\delta V - \delta B$ alignment using direct and independent measurements of velocity and magnetic fields, and (ii) report distinctive plasma kinetic signatures within the Alfvén vortex. The connection between coherent Alfvén vortex and plasma kinetic effects is thus confirmed. Implications for the local energy conversion associated with the pressure-strain interaction are discussed.

2. Event Overview

We choose an interval during 10:50–11:20 UTC on 2015 October 2, where MMS is located in the turbulent magnetosheath. The magnetic and electric field data are from the Flux Gate Magnetometer (FGM), Search Coil Magnetometer (SCM), and the Electric Double Probes installed on the FIELDS suite, respectively (Ergun et al. 2016; Russell et al. 2016; Torbert et al. 2016). The 3D particle data, in the form of ion and electron VDFs and the associated plasma moments (i.e., density, velocity, temperature, and pressure), are from the Fast Plasma Investigation (Pollock et al. 2016). In the GSE coordinates, the magnetic field is generally stable around $B_0 = 39.2 \ (-0.56, 0.82, 0.13) \ $ nT throughout the interval as shown in Figure 1(a), while a few discontinuities with the increase of B_z and decrease of B_x and B_y can be spotted. The mean flow speed is around $V_0 = 170 \ (-0.7, 0.7, -0.1) \ km \ s^{-1}$ and it has an angle of about $35°$ with respect to B_0. The total magnetic field fluctuations energy, which is used to select the interval of interest, exhibit large variations as plotted in Figure 1(b). The sub-interval marked in cyan contains the structure of interest and it will be further analyzed in more detail. The relevant plasma parameters during these two intervals are listed in Table 1. To quantify the turbulence energy across different scales, Figure 1(d) presents the trace of the power spectrum density (PSD) of the magnetic field. The black curve presents the results for the total magnetic field during the 30-minute interval. It can be seen that the PSD follows a power law $f^{-1.8}$ at [0.06, 0.38] Hz, suggesting a fluid-like behavior in the inertial range. Then it steepens and follows f^{-3} between [0.4, 3] Hz, where the spectral break generally matches with the proton cyclotron frequency f_{cp} and the Doppler-shifted proton inertial length f_{di}, under the assumption of wave vectors parallel to the plasma flow. Notice that the perpendicular ion plasma beta $\beta_{\perp i} = (\rho_i / d_i)^2$ is of the order of one in our event, thus f_{di} and the Doppler-shifted proton gyroradius $f_{\rho p}$ cannot be separated easily. Finally, the PSD steepens again and follows $f^{-3.9}$ between [4, 70] Hz.
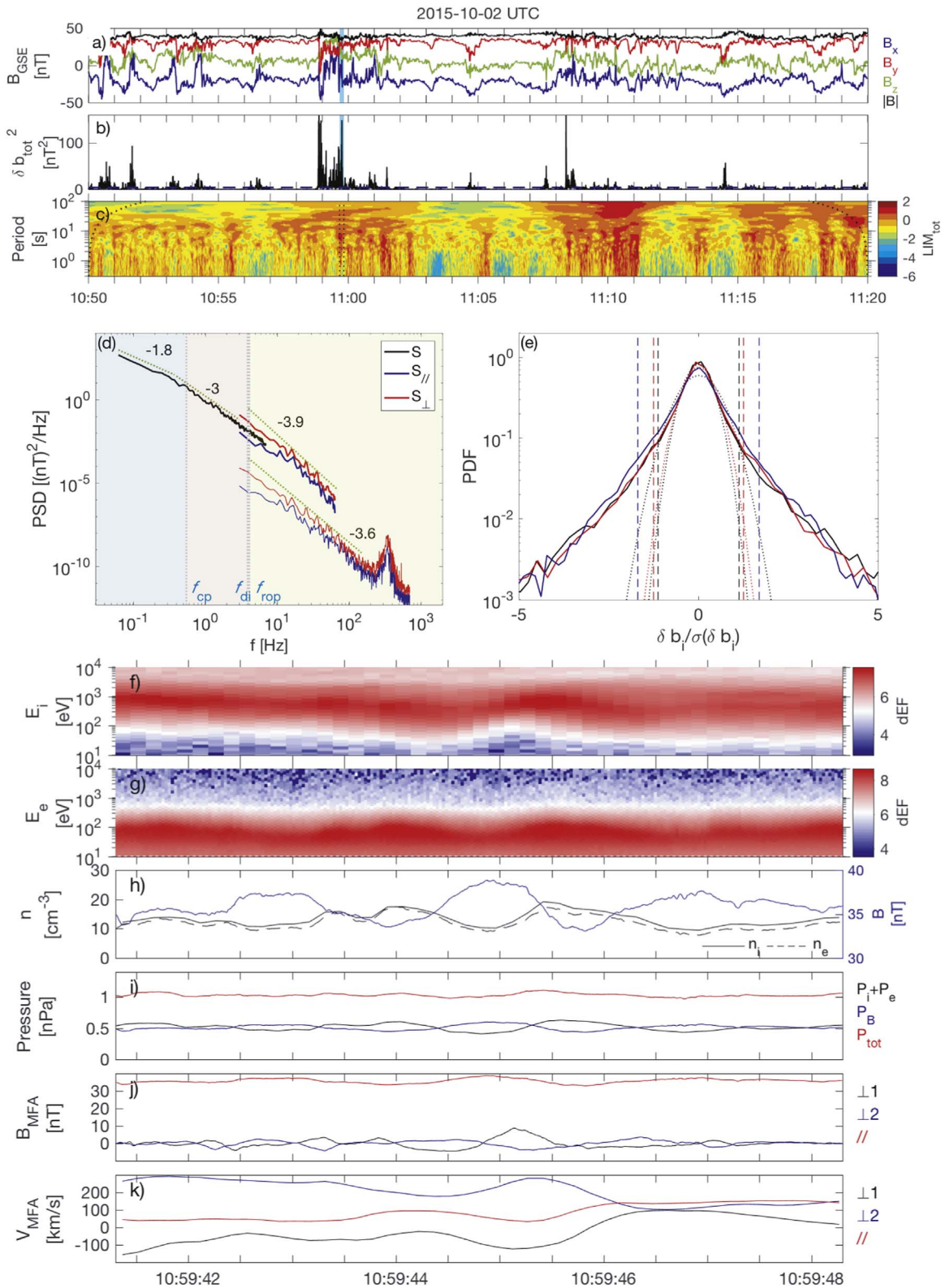
Figure 1. Overview of the event. (a) Magnetic field in GSE coordinates and its magnitude during a 30-minute interval on 2015 October 2. (b) Total turbulent magnetic energy at ion scales (0.4–3 Hz), where the horizontal blue dashed line indicates the threshold energy for the selection of intermittent intervals. The 7 s sub-interval marked by a cyan shadow contains the structure of interest. (c) Logarithmic of LIM_{total}. (d) PSD of the total magnetic field fluctuations during 10:50:00–11:20:00 UT (black curve), together with the PSDs (up to 700 Hz) of the parallel (blue) and perpendicular (red) magnetic field fluctuations during 10:59:41.5–10:59:48.5 UT. The spectra at $0.04 < f < 60$ Hz are calculated from FGM data, and the spectra at $3 < f < 700$ Hz are calculated from SCM data. Note that the original spectra at $f > 3$ Hz overlap with each other, thus the spectra based on SCM has been vertically shifted for better comparison. (e) PDFs of the normalized ion-scale magnetic field fluctuations in the GSE coordinates, overplotted with the corresponding Gaussian distributions (dotted curves) and three standard deviations of each fit (vertical dashes). The close-up overview of the cyan shadowed interval includes: (f) ion energy spectrogram; (g) electron energy spectrogram; (h) ion and electron density vs. magnetic field strength; (i) magnetic pressure, plasma pressure, and total pressure; (j) magnetic field in MFA coordinates; (k) velocity field in the MFA coordinates.

Table 1
Plasma Parameters during the Intervals of Interest

	Interval 1 (UT) 10:50:00–11:20:00	Interval 2 (UT) 10:59:41.5–10:59:48.5
$\boldsymbol{B}$ (nT)	39 (−0.56, 0.82, 0.13)	36 (−0.34, 0.81, 0.47)
$\boldsymbol{V}$ (km s^{-1})	170 (−0.7, 0.7, −0.1)	242 (−0.7, 0.5, −0.5)
θ_{BV} (degree)	35	67
N (cm^{-3})	14	13
T_i (eV)	198	216
T_e (eV)	31	31
$T_{i,\parallel}/T_{i,\perp}$	0.8	1.0
$T_{e,\parallel}/T_{e,\perp}$	1.4	1.7
β_i	0.7	0.9
β_e	0.1	0.1
ρ_p (km)	55	60
d_i (km)	60	62
$f_{cp}, f_{\rho p}, f_{di}$ (Hz)	0.59, 2.9, 2.7	0.55, 4.0, 3.9

For the transition range around ion scales, the turbulent energy is believed to further cascade and the kinetic physics begins (Alexandrova et al. 2013; Kiyani et al. 2015). Various forms of coherent structures (i.e., current sheet, vortex filaments) are usually found to reside near this range (i.e., between the end of the MHD range and proton scales in Lion et al. 2016; Perrone et al. 2016, 2017). Hence, in the following analysis we focus on fluctuations of similar scales, where the frequency ranges is chosen as [0.4, 3] Hz, and the timescale is [0.3, 3] s. It has been shown recently that, in case of a collisionless turbulent system as the solar wind, the intermittency, non-Gaussian fluctuations, and phase coherence of magnetic field components are interrelated (Perrone et al. 2017). We expect this relation to be present here and thus take similar procedures as in Perrone et al. (2017) to search for the intermittent events. The first step is to reconstruct the fluctuations using the bandpass filter based on wavelet transforms (Torrence & Compo 1998; He et al. 2012; Wang et al. 2014; Perrone et al. 2016). The magnetic field fluctuations are thus defined as

$$\delta b_i(t) = \frac{\delta j \delta t^{1/2}}{C_\delta \psi_0(0)} \sum_{j=j1}^{j2} \frac{\widehat{\mathcal{W}_i}(\tau_j), t)}{\tau_j^{1/2}}, \qquad (1)$$

where i represent the magnetic field components, j represent the scale index, δj is the constant scales step, $\widehat{\mathcal{W}_i}$ is the real part of the wavelet coefficient $\mathcal{W}_i$, $C_\delta = 0.776$. ψ_0 is the Morlet mother function and $\psi_0(0) = \pi^{-1/4}$ at time $t = 0$ (Torrence & Compo 1998), τ_{j1} and τ_{j2} are taken to be 0.3 and 3 s, respectively. The second step is to determine the threshold energy as defined by $\varepsilon_T = \sum_{i=1}^{3}(3\sigma_G(\delta b_i))^2$, where $\sigma_G(\delta b_i)$ is the standard deviation of the Gaussian fit for each magnetic field fluctuation component. $\sigma_G(\delta b_i)$ are fitted to be 0.36, 0.32, and 0.49 nT, leading to a $\varepsilon_T \sim 4.3$ nT^2. From a statistical point of view, 99.7% of all the values in Gaussian distribution are within $3\sigma_G(\delta b_i)$ from the mean. In other words, the events whose total energy $\delta b_{\text{tot}}^2 = \sum_{i=1}^{3}(\delta b_i)^2$ are larger than ε_T could contribute to the non-Gaussian part of the distributions. Figure 1(e) presents the PDFs of the normalized magnetic field fluctuations $\delta b_i/\sigma(\delta b_i)$ together with their Gaussian fits. The presence of clear non-Gaussian tails suggest the abundance

of intermittent events during the whole interval. The last step is to locate these events. As seen in Figure 1(b), there are approximately 14 events (with at least 10 s in duration) with δb_{tot}^2 larger than 5 nT^2. We have picked one interval during 10:59:41.5–10:59:48.5 UT for further study. This event is characterized by large magnetic energy ∼150 nT^2 and strong flow vorticity up to ∼1.4 /s as compared to the mean value of ∼0.4 /s. Furthermore, the local intermittency measure (LIM) exhibits an extension of temporal scale from several tens of seconds to sub-seconds, as seen in the LIM$_{\text{total}}$ of Figure 1(c). The LIM spectrogram, as a function of time and scales, is computed as the instantaneous energy of fluctuations normalized to its mean value over the studied time interval (Farge 1992):

$$\text{LIM}_{\parallel,\perp,\text{total}} = |\mathcal{W}_{\parallel,\perp,\text{total}}|^2 \big/ \langle|\mathcal{W}_{\parallel,\perp,\text{total}}|^2\rangle_t. \qquad (2)$$

where $|\mathcal{W}_{\text{total}}|^2 = |\mathcal{W}_\parallel|^2 + |\mathcal{W}_\perp|^2$ is the total fluctuation energy. For the coherent structures (space or time localized energetic events), one of its intrinsic properties is the energy coupling over many scales (Farge 1992; Frisch 1995), which is usually manifested in the spanning of LIM at a wide range of spatial scales (or temporal scales if the Taylor frozen-in hypothesis is assumed; Lion et al. 2016; Perrone et al. 2017). While for the wave phenomenon, the energy distribution is typically focused around a certain frequency, i.e., Alfvén ion cyclotron (Alexandrova et al. 2004) or electron cyclotron waves (Lacombe et al. 2014). Therefore, the extension of LIM provides evidence of coupling from MHD to sub-ion scales and hence implies the presence of a coherent structure (Farge 1992; Frisch 1995; Lion et al. 2016; Perrone et al. 2017). Note that because LIM$_\parallel$, LIM$_\perp$, and LIM$_{\text{total}}$ exhibit nearly the same features in this event, only LIM$_{\text{total}}$ is presented here.

The overview of this 7 s event is presented in Figures 1(f)–(k), together with the PSDs of the perpendicular and parallel magnetic field fluctuations (denoted as $S_\perp$ and $S_\parallel$ displayed in Figure 1(d). The ion and electron differential energy spectrograms exhibit fluctuations in their energy levels and magnitudes (Figures 1(f) and (g)), in correspondence with the density variations (Figure 1(h)). However, the total pressure is almost stable, where the plasma pressure is balanced by the magnetic pressure (Figure 1(i)). Interestingly, large-amplitude magnetic field fluctuations (>10 nT) and velocity fluctuations (>50 km s^{-1}) are found to be localized in time (within 6 s). In addition, these fluctuations are dominant in the perpendicular direction as seen in Figures 1(j) and (k) ($\delta B_\perp/B_0 \sim 0.37$, $\delta B_\parallel/B_0 \sim 0.1$, $\delta V_\perp/V_A \sim 0.38$, $\delta V_\parallel/V_0 \sim 0.1$). The time series are presented in the mean field-aligned (MFA) system, where the z direction corresponds to a 3 s running averaged of the magnetic field in the GSE coordinates, the y direction is obtained from the cross product of the z vector and the spacecraft location in the GSE coordinates, and the x direction is the cross product of y and z directions. Moreover, the slope for the perpendicular fluctuations are close to −4 (i.e., −3.6 for the result based on FGM and −3.9 for the result based on SCM). These features give some hint to the presence of the incompressible Alfvén vortex structure. This structure has localized in space strong perpendicular magnetic field fluctuations and a theoretical −4 slope for the PSD, due to the discontinuity of the parallel current density at the vortex boundary (Alexandrova 2008). Notice that the "bump" in the
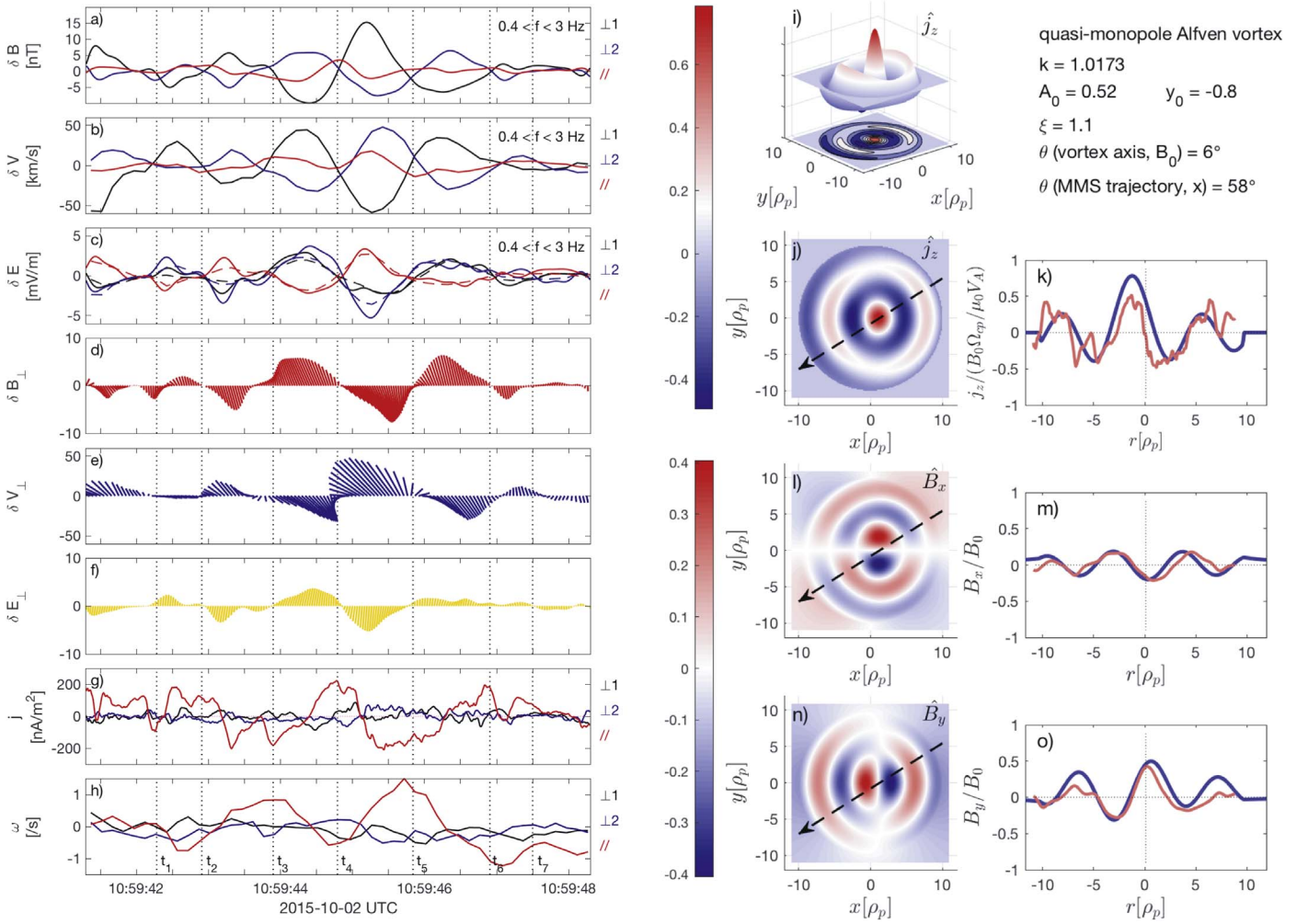
Figure 2. Identification of the Alfvén vortex. (a) Magnetic field fluctuations in MFA coordinates. (b) Same as (a), here for the velocity field. (c) Same as (a), here for the electric field. The solid lines represent direct δE measurements, while the dashed lines correspond to $-\delta(V_i \times B)$. (d) Hodogram demonstrations of perpendicular magnetic field. (e) Same as (d), here for the velocity field. (f) Same as (d), here for the electric field. (g) Current density in the MFA coordinates. (h) Flow vorticity in the MFA coordinates calculated from ion velocity. Seven times (from t_1 to t_7) within the vortex are marked as vertical dashed lines. (i) 3D representation of the current density pattern based on dipolar Alfvén vortex model, with its parameters listed on the right side. (j) Parallel current pattern overplotted with the spacecraft trajectory. (k) Comparison between the vortex solution with the MMS observation for the parallel current. Note that the current is normalized by $B_0\Omega_{cp}/\mu_0 V_A$, the magnetic field is normalized by mean magnetic field B_0, the spatial lengths are normalized by proton gyroradius ρ_p, and the time series from MMS has been transferred to a spatial series based on the timing results of around 200 km s^{-1}. (l) Same as (j) but for $B_{\perp 1}$. (m) Same as (k) but the $B_{\perp 1}$. (n) Same as (j) but for $B_{\perp 2}$. (o) Same as (k) but for $B_{\perp 2}$.

PSD near the electron cyclotron frequency corresponds to parallel whistler emissions within the structure, which is out of the scope of the present Letter but it will be studied in a future work.

3. Kinetic Signatures in the Alfvén Vortex

3.1. Identification of the Alfvén Vortex

To better determine the nature/type of this structure, we present more detailed analysis of the small-scale electromagnetic and velocity field, as well as current density, flow vorticity, in Figures 2(a)–(h). As seen in Figures 2(a)–(c), during the interval that starts from t_1 and terminates at t_7, the perpendicular components of δB, δV, and δE exhibit five polarity reversals marked as t_2, t_3, …, t_6. The variations of the field direction, also revealed in feather plots of the $\delta B_\perp$, $\delta V_\perp$, $\delta E_\perp$ (Figures 2(d)–(f)), are reminiscent of vortices. The directional changes of $\delta B_\perp$ and $\delta V_\perp$ correspond to the extrema of the parallel current density $j_\parallel$ and flow vorticity $\omega_\parallel$, which are

much larger than $j_\perp$ and $\omega_\perp$ (Figures 2(g) and (h)). Here the current and vorticity are calculated by applying the curlometer method to the magnetic and ion velocity field, respectively (Dunlop et al. 2002), where the validity of the methods has been verified in recent MMS observations of ion-scale currents (Dong et al. 2018). In addition to the perpendicular field reversals, we observe clear anti-correlation of $\delta B_\perp$ and $\delta V_\perp$, satisfying the relation $\delta V_\perp / V_A = -\xi \delta B_\perp / B_0$, where $\xi_{\perp 1}$ is ~1.14 and $\xi_{\perp 2}$ is ~1.03 for the two perpendicular directions. The small difference between the two coefficients may be related to linear regression error, which is ~0.1 in this case. The unique $\delta B_\perp$, $\delta V_\perp$, $j_\parallel$, and $\omega_\parallel$ features indicate again the presence of a coherent Alfvénic vortex, which manifests itself as a 2D tube-like structure with quasi-field-aligned current (Alexandrova et al. 2006). In addition, the direct δE observation (solid lines in Figure 2(c)) nearly match with $\delta E = -\delta(V_i \times B)$ (dashed lines in Figure 2(c)), which verifies the assumption that the electric field at scales of the Alfvén vortex can be approximated by the convection term of Ohm's law (Alexandrova et al. 2006).

To provide more evidence for the existence of Alfvén vortex, we first obtain the orientation and motion of the structure from four spacecraft measurements, and then compare the observations with Alfvén vortex solutions to determine more parameters of the vortex (e.g., type, inclination, radius). Here the timing method (Schwartz 1998; Alexandrova et al. 2006) is used to calculate the normal direction n and the propagation velocity V_n, where the accuracy is guaranteed by the clear time shift (~ 0.1 s) of the signals measured by four spacecraft with separations ~ 20 km. The inferred angle between $\boldsymbol{n}$ and the local $\boldsymbol{B}_0$ is around $86°.8$. This result is in contrast with the minimum variance analysis (MVA) from single spacecraft measurements, which gives a normal (or wave vector) direction nearly parallel to $\boldsymbol{B}_0$ ($\theta_{k,B_0} \sim 8 \pm 5°$). Indeed, the difference of the "normal" directions from different methods favors the presence of a localized cylindrical vortex rather than a parallel propagating plane wave. For this tube-like topology, its axis is given by the minimum variance direction (i.e., along $\boldsymbol{B}_0$), while the normal of its surface is given by the timing results (i.e., perpendicular to B_0). In addition to this, the propagation velocity V_n is $\sim (70, 189, 18) \pm 20$ km s^{-1} in the MFA frame, and the perpendicular velocity $V_\perp n$ is $\sim (70, 190, 0) \pm 20$ km s^{-1}, which is slightly larger than the perpendicular flow speed $(25, 190, 0)$ km s^{-1}. Hence, the vortex barely propagates in the plasma rest frame (with the perpendicular propagation speed $u_\perp \sim 45 \pm 20$ km s^{-1}, $u_\perp / V_A \sim 0.18 \pm 0.08$).

Among various models describing the localized Alfvén vortex filaments, one simple case is the specific nonlinear solutions of the ideal incompressible MHD system (Petviashvili & Pokhotelov 1992; Alexandrova 2008; Jovanovic et al. 2017), which satisfies the generalized Alfvén relation

$$\psi \propto \xi A. \tag{3}$$

Here ψ is the flux function, which relates to the transverse velocity fluctuations $\delta V_\perp = z \times \nabla \psi$, A is the magnetic potential, which relates to the transverse magnetic fluctuations $\delta B_\perp = \nabla A \times z$, and z is the magnetic field direction.

The Alfvén vortex solution in the vortex plane (x, η) reads

$$\begin{cases} A = A_0(J_0(kr) - J_0(ka)) + \dfrac{u}{\xi}\dfrac{x}{kr}\left(kr - 2\dfrac{J_0(kr)}{J_1(ka)}\right), & r < a \\ A = a^2 \dfrac{u}{\xi}\dfrac{x}{r^2}, & r \geqslant a. \end{cases} \tag{4}$$

The analytical expression depends on the axial distance to the vortex center $r = \sqrt{x^2 + \eta^2}$, where η is defined as $\eta = y + uz/\xi - ut$, with u being the vortex propagation speed in the vortex plane (x, η). If the angle between the vortex axis and background magnetic field $\boldsymbol{B}_0$ is θ_{vortex}, then ξ is defined as $\xi = u/\tan(\theta_{\mathrm{vortex}})$. Inside the vortex core ($r < a$), the first term, in the form of the Bessel function of zeroth order J_0, describes the monopole component with an arbitrary amplitude A_0. The second term, in the form of Bessel function of the first order J_1, describes the dipolar components relating to the vortex inclination/propagation effects. The amplitude of the dipolar component depends on u/ξ that is $\tan(\theta_{\mathrm{vortex}})$. Outside the vortex core ($r > a$), the only dipole component is nonzero and it decays at infinity as a power law $\sim 1/r$. Note that the continuity of the solution at $r = a$ requires $J_1(ka) = 0$. In the limit of $u = 0$, the solution is axial symmetric and the vortex is a strictly field-aligned monopole. In the limit of

$A_0 = 0$, the solution is axial asymmetric and the vortex is a strictly dipole. Under other circumstances, the combined solution of the two terms in Equation (4) depicts a mixed scenario (e.g., monopole sitting on a dipole).

We choose the quasi-monopole model to fit the data as the observed time series of $j_\parallel$ appears to be symmetric around the half-time of the interval, resembling the monopole configuration. In addition, we also consider the propagation effect by choosing the nonzero angle between the vortex axis and $\boldsymbol{B}_0$, which is different from the strictly aligned case for the monopole. In particular, the vortex diameter is estimated to be around $20\,\rho_p$ to match the timing results of ~ 1200 km. The third zero of the Bessel function is selected ($ka = 10.17$) to approximate the triple peaks of the current density. The angle between the vortex axis and $\boldsymbol{B}_0$ is chosen as $\theta_{\mathrm{vortex}} \sim 6°$, nearly in agreement with the MVA analysis. We note that the perpendicular speed of the vortex $u_\perp = \tan(\theta_{\mathrm{vortex}})V_A \simeq 0.13 \pm 0.09\,V_A$, as well as the angle of the MMS trajectory $\theta_{\mathrm{MMS}} \sim 58°$, are in qualitative agreement with the timing results of $0.18 \pm 0.08\,V_A$, and $69°$, respectively, suggesting the self-consistency of the fitting process. The modeled current and magnetic field results are shown in Figures 2(i)–(n), with the dashed lines representing the virtual trajectory of MMS, and the parameters listed on the right-hand side of Figure 2(i). It can be seen from Figures 2(i) and (j) that the current has three positive peaks and two negative peaks located at the edge ($r \sim 10\,\rho_p$), center ($r \sim 0\,\rho_p$), and middle part ($r \sim 3\,\rho_p$) of the vortex. As a result, three layers of the azimuthal magnetic field are visible within the vortex, which agree with the B_x, B_y contours in Figures 2(l) and (n). The pattern for the quasi-monopole solution here closely resembles the circular symmetric monopolar solution, but for a slight asymmetry along the $x = 0$ axis. This is attributed more to the major influence from the first term (symmetric) in the vector potential (see Equation (4)) than the minor, asymmetric effect from the second term. Figures 2(k), (m), (o) present the direct comparison between the modeled results and the observation. The agreement between the two results confirms the feasibility of the quasi-monopole description for the observed Alfvén vortex.

3.2. Kinetic Signatures within the Alfvén Vortex

Now that we have gained the geometrical properties of the Alfvén vortex, it is thus possible to study the plasma features at different locations within it. To underline the specific observation made at certain location, Figure 3 begins with the same current density and vorticity as in Figure 2, and then present the temperatures as well as the VDFs for ions and electrons, respectively. In addition, the vertical dashed lines are kept the same as Figure 2 so as to mark the different times and locations within the vortex, where t_1 and t_7 correspond to outer edge (r_3), t_2 and t_6 correspond to the inner edge (r_2), t_3, and t_5 correspond to the middle (r_1), and t_4 corresponds to the center (r_0) of the vortex.

Three distinct temperature features in association with the strong magnetic/velocity field gradient can be identified. (1) There is a correlation between the total ion/electron temperature and parallel current density $j_\parallel$/vorticity $\omega_\parallel$. Ions are relatively hotter (~ 260 eV) near r_2 and r_0, when $j_\parallel$ reaches its local maxima, yet their temperatures are colder (~ 180 eV) near r_1, when $j_\parallel$ is at its local minima. In contrast, electrons are relatively colder (~ 25 eV) at $j_{\parallel,\mathrm{max}}(\omega_{\parallel,\mathrm{min}})$, and are hotter ($\sim 60$ eV) at $j_{\parallel,\mathrm{min}}(\omega_{\parallel,\mathrm{max}})$. (2) The temperature anisotropy
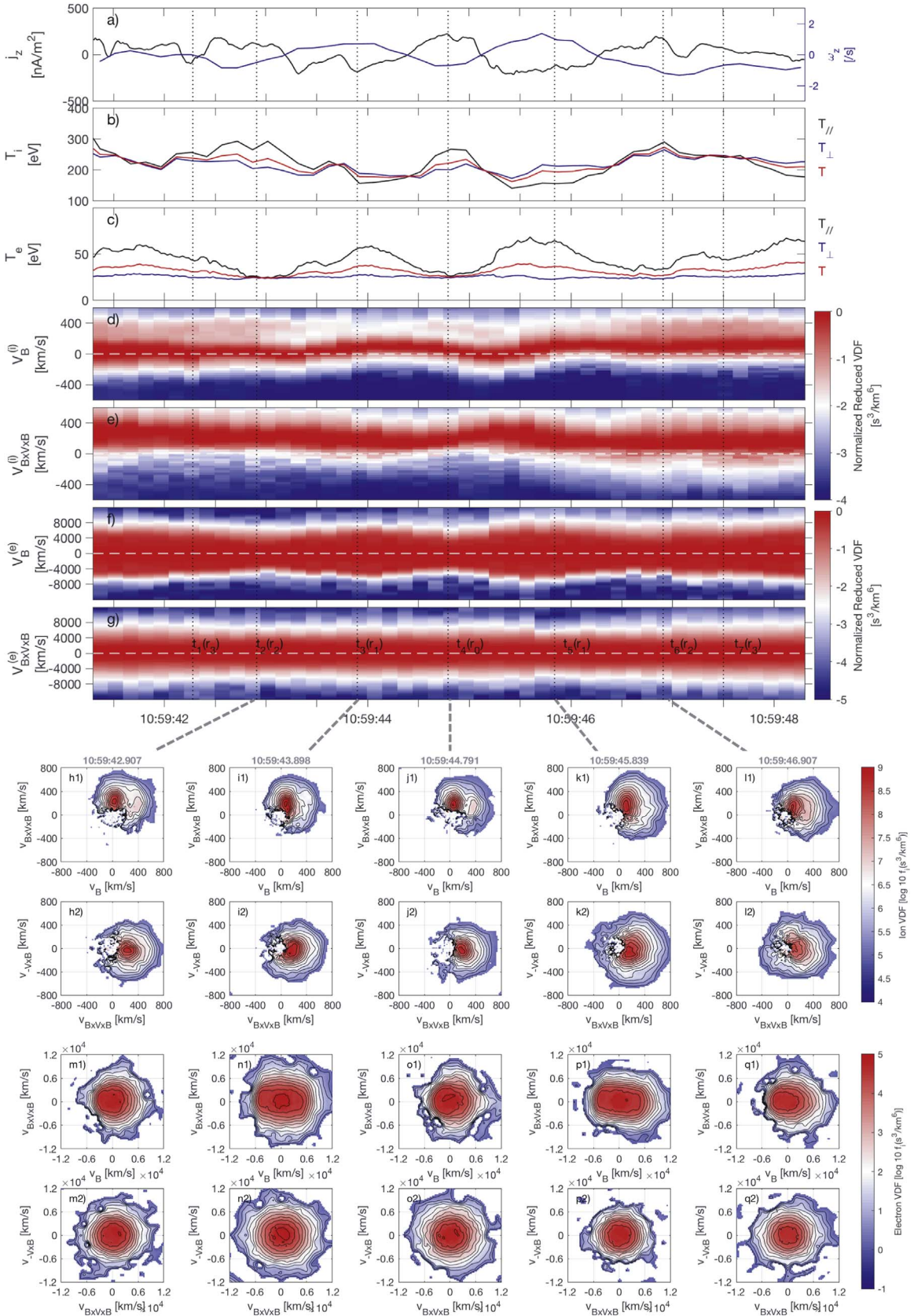
Figure 3. Kinetic signatures observed in the Alfvén vortex. (a) Current density vs. flow vorticity in the MFA coordinates. (b) Ion parallel, perpendicular and total temperature. (c) Same as (c) but for electrons. (d) Normalized reduced ion velocity distribution functions (NR-iVDFs) in the parallel direction. (e) Same as (d) but in the perpendicular direction. (f) Normalized reduced electron velocity distribution functions (NR-eVDFs) in the parallel direction. (g) Same as (f) but in the perpendicular direction. (h1)—(l1) Projection of the ion velocity distribution functions (iVDFs) in the local $(B, B \times V \times B)$ plane, taken during the times marked by the vertical dotted lines. (h2)–(l2) Projection of the iVDFs in the local $(B \times V \times B, -V \times B)$ plane. (m1)–(q1) Same as (h1)–(l1) but for electrons. (m2)–(q2) Same as (h2)–(l2) but for electrons. Note that the projection of VDFs on planes constructed by B_0, V_0 exhibit similar features as compared to the results shown here.
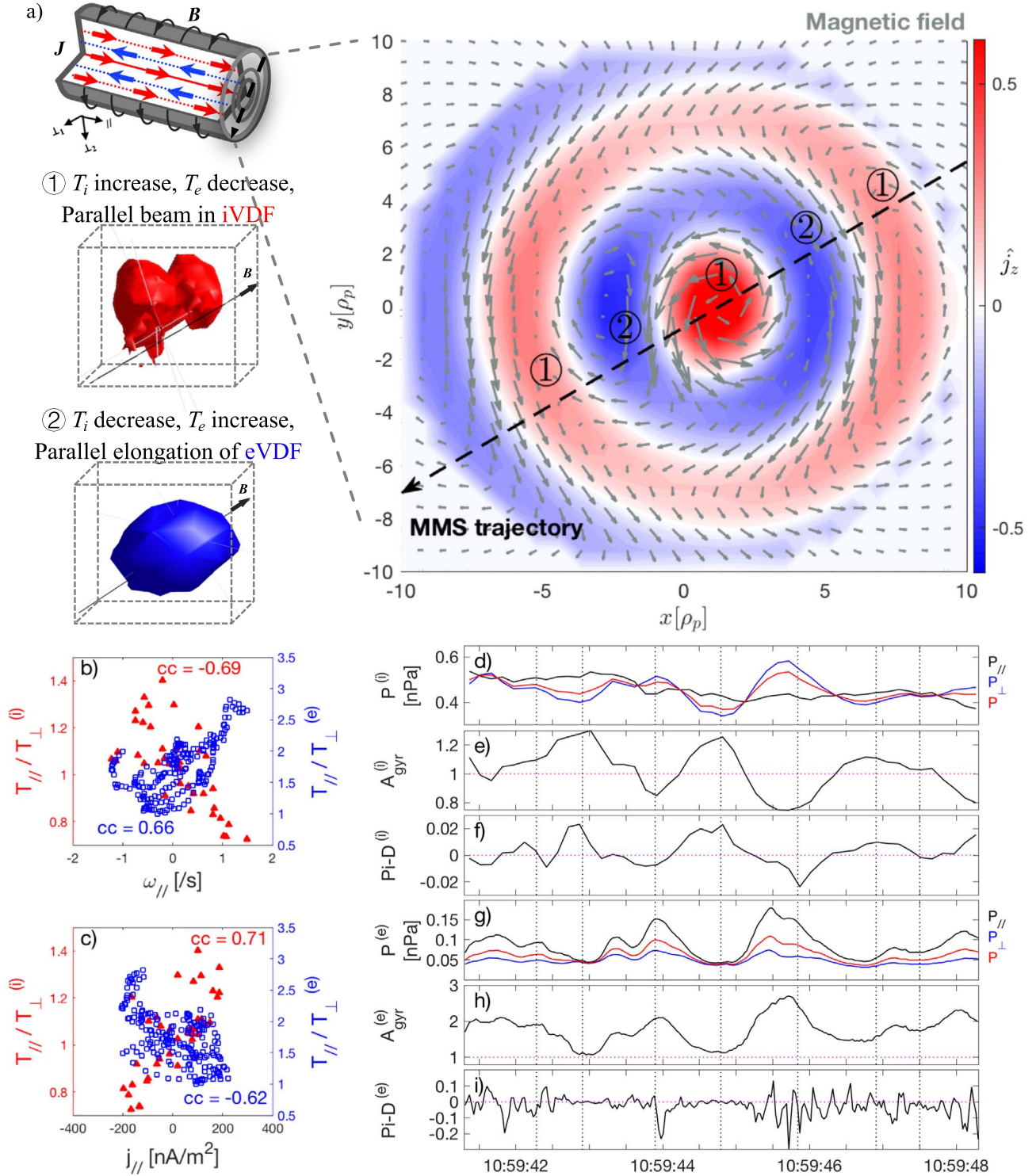
Figure 4. Illustration of the kinetic signatures within the Alfvén vortex. (a) The geometry, electromagnetic field, velocity field of the vortex, together with the 3D view of two non-Maxwellian velocity distribution functions. (b) Scatter plot of parallel vorticity vs. ion and electron temperature anisotropy. (c) Scatter plot of parallel current density vs. ion and electrons temperature anisotropy. (d) Ion parallel, perpendicular, and total pressure. (e) Ion gyrotropic pressure anisotropy $A_{\mathrm{gyr}}^{(i)} = P_\parallel/P_\perp^{(i)}$. (f) Ion pressure-strain interaction term $P_i - D^{(i)}$. (g)–(i) Same as (d)–(f) but for electrons.

$T_\parallel/T_\perp$ is correlated with $j_\parallel(\omega_\parallel)$ (see Figures 4(b) and (c)). At locations near r_2 and r_0, $T_\parallel$ is larger than $T_\perp$ for ions, while $T_\parallel$ and $T_\perp$ are almost the same for electrons. At locations near r_1, $T_\parallel$ is smaller than $T_\perp$ for ions, while $T_\parallel$ is larger than $T_\perp$ for electrons. (3) The electron temperatures behave in an opposite trend as compared with ions, which may reflect a balanced

energy allocation between these two components. In addition, the redistribution of energy mainly happens in the parallel direction.

Ion energization and anisotropization has been revealed to occur near, but not centered on, current structures in recent 2D hybrid simulations and theories (Del Sarto et al. 2016;

8

Franci et al. 2016; Parashar & Matthaeus 2016; Valentini et al. 2016). To our knowledge, the MMS observations reported here provide the first evidence of plasma temperature anisotropy inside the vortex structure. The ions' behaviors, in particular, verify the correlation between temperature anisotropy and the out-of-plane vorticity observed in Franci et al. (2016), Parashar & Matthaeus (2016), and Valentini et al. (2016). In these studies, due to the different spatial distribution of the vortex and the current sheets (i.e., the vorticity is less filamentary then the current sheets and sometimes eddies are formed on the flank of the planar current sheets), the ion temperature anisotropy displays different correlation with $|\omega_\parallel|$ than with $|j_\parallel|$ (Franci et al. 2016; Parashar & Matthaeus 2016). For the vortex of Alfvénic nature reported here, however, we have explored another scenario where the anti-phased perpendicular magnetic and velocity field implies the alignment of vorticity and current density, hence the correlation between ion temperature anisotropy with $|\omega_\parallel|$ and $|j_\parallel|$ should be the same.

For a more delicate view of the plasma characteristics, Figures 3(d)–(g) plot the time variation of the normalized reduced distribution functions (NR-VDFs) for ions and electrons, respectively. The reduction process along $\boldsymbol{B}$ direction is achieved by double integration of the distribution functions in the $-\boldsymbol{V} \times \boldsymbol{B}$ and $\boldsymbol{B} \times \boldsymbol{V} \times \boldsymbol{B}$ direction. Likewise, the reduction along $\boldsymbol{B} \times \boldsymbol{V} \times \boldsymbol{B}$ is obtained from the double integration of the VDFs in the $\boldsymbol{B}$ and $-\boldsymbol{V} \times \boldsymbol{B}$ directions. The normalization is then completed by dividing the reduced VDFs by their maximum value. First, the NR-VDFs for the ion are examined in Figures 3(d) and (e). As shown in Figure 3(d), the NR-iVDFs along $\boldsymbol{B}$ are changing dynamically with the broadening and narrowing in the velocity width taking place alternatively. This corresponds to the parallel temperature variations shown in Figure 3(b). Moreover, beam-like populations drifting at velocity of $\sim$300–400 km s^{-1} (in comparison with the local Alfvén speed $\sim$250 km s^{-1}) are found to appear near r_2 and r_0. This minor population could contribute up to 10% of the major NR-iVDFs centered at $V_B = 0$ and thus lead to an asymmetry of the NR-iVDFs with respect to $V_\parallel = 0$. As revealed in Figure 3(e), the NR-iVDFs along $\boldsymbol{B} \times \boldsymbol{V} \times \boldsymbol{B}$ are centered at 200 km s^{-1}, which corresponds to the $\boldsymbol{E} \times \boldsymbol{B}$ convection motion. In addition, a slight broadening is visible near r_1 and it agrees with the perpendicular temperature increase in Figure 3(b). Next, the electron observations are presented in Figures 3(f) and (g). As seen in Figure 3(f), the NR-eVDFs along $\boldsymbol{B}$ exhibit significant variations in the velocity width, but their symmetries with $V_\parallel = 0$ are maintained. In addition, the broadening near r_1 and narrowing near r_2 and r_0 is in reverse trend as compared with NR-iVDFs. The NR-eVDFs along $\boldsymbol{B} \times \boldsymbol{V} \times \boldsymbol{B}$ in Figure 3(g) stay mostly stable, which explains the generally constant behavior of the perpendicular electron temperature. Last, we note that in addition to the results shown in the above two directions, the NR-VDFs along $-\boldsymbol{V} \times \boldsymbol{B}$ for both ions and electrons remain nearly unchanging during the whole interval, which can be partly shown as below.

To highlight the distinctive VDFs within the vortex, we show five columns of the VDFs (five snapshots from t_2 to t_6) in different planes constructed by local $\boldsymbol{B}$, $\boldsymbol{B} \times \boldsymbol{V} \times \boldsymbol{B}$, and $-\boldsymbol{V} \times \boldsymbol{B}$ directions. Four types of VDFs can be identified. (1) The iVDFs display beam-like structures on the positive $V_\parallel$ side of the distribution at t_2 (Figure 3(h1)), t_4 (Figure 3(j1)). These beams seem to partially merge with the major population at t_6

(Figure 3(l1)). (2) The perpendicular broadenings of the iVDFs in the $\boldsymbol{B} \times \boldsymbol{V} \times \boldsymbol{B}$ direction are evident at t_3 (Figure 3(i1), (i2)) and t_5 (Figure 3(k1), (k2)). (3) The eVDFs display clear elongation on both the positive and negative side of the parallel direction at t_3 (Figure 3(n1)) and t_5 (Figure 3(p1)), with the appearance of bidirectional beam-like structures at $v \sim 6000$ km s^{-1}. (4) The eVDFs are generally isotropic at t_2, t_4 (Figure 3(m1), (o1), (m2), (o2)), and are slightly anisotropic at t_6 (Figure 3(q1), (q2)). If examine more carefully at these times, it can be found that the contours of eVDFs in the anti-parallel direction are closer than the ones in the positive direction (see the dense contours at $v \sim -4000$ km s^{-1} in Figure 3(m1), (o1), (p1)). This has led to a net negative electron drift velocity that is much larger than the ion parallel velocity, and thus are responsible for the parallel current near r_0 and r_2. In particular, the snapshots of eVDFs presented here are reminiscent of the electron distributions observed in a fast solar wind event by Perrone et al. (2017), where the authors have reported an isotropic distribution in the vortex center and an increased phase space density at the vortex boundary. However, the anisotropic characteristics are somehow different as the "strahl" populations from the background solar wind, which affect the distribution in the parallel direction, are always present in Perrone et al. (2017).

4. Energy Conversion Channels Associated with the Alfvén Vortex

The deformation of the particle distributions, as seen in both gyrotropic and non-gyrotropic temperature anisotropy, have been reported in space observations and simulations of plasma turbulence (Marsch et al. 1982; Valentini et al. 2011; Servidio et al. 2012; Perrone et al. 2013; He et al. 2015b; Franci et al. 2016). Despite the active debate concerning the kinetic scale nature of the turbulence (i.e., waves and/or structures in Groselj et al. 2018), two types of mechanisms have been widely invoked to explain such phenomenon. One is wave-particle interactions, such as cyclotron and Landau resonances with kinetic Alfvén and slow-mode waves (He et al. 2015a, 2015b). In a more recent paper, modulations of the ion and electron pitch angle in the presence of large-amplitude electromagnetic waves are also found (Zhao et al. 2018). The other is dissipation near coherent structures (Osman et al. 2012b; Wan et al. 2012; Pezzi et al. 2016). This mechanism is related to gradients in the magnetic/velocity field, or more specifically, the work done by the pressure-strain interaction $-(\boldsymbol{P} \cdot \boldsymbol{\nabla}) \cdot \boldsymbol{u}_F$, which can be decomposed into the isotropic compression term $-p\theta$ and traceless pressure-strain interaction term $-\Pi_{ij}D_{ij}$. Here $\boldsymbol{P}$ is the pressure tensor, $\boldsymbol{u}_F$ is the bulk flow velocity, $p = 1/3 P_{ii}$ is the scalar pressure, $\theta = S_{ii}$ is the trace of the strain rate tensor, $\Pi_{ij} = P_{ij} - 1/3 P_{ii}\delta_{ij}$ is the traceless pressure tensor, $D_{ij} = S_{ij} - 1/3 S_{ii}\delta_{ij}$ is the traceless strain rate tensor, $S_{ij} = 1/2(\partial_i u_j + \partial_j u_i)$ is the symmetric strain rate tensor, and δ_{ij} is the Kronecker delta. As shown in fully kinetic simulations, the pressure work could trigger individual energy conversion channels (for both ions and electrons) between fluid energy and random thermal energy (Yang et al. 2017a, 2017b). This idea has been tested in a few current layers (see the MMS observation of electron energy conversion channel in Chasapis et al. 2018). More importantly, theoretical models have proved recently that the momentum anisotropy contained in a sheared flow could lead to proton pressure anisotropy from an initial isotropic state (Cerri et al. 2013; Del Sarto et al. 2016; Del Sarto & Pegoraro 2018). To be more precise, the evolution of

gyrotropic and non-gyrotropic anisotropies are driven by $-\Pi_{ij}D_{ij}$ term, while the compression term seems not to contribute (Del Sarto & Pegoraro 2018).

To find a possible interpretation for the observed pressure anisotropies, we have thus investigated the ion and electron $-\Pi_{ij}D_{ij}$ terms within the vortex (denoted as $P_i - D^{(i)}$ and $P_i - D^{(e)}$, respectively). The stress tensor is obtained using the curlometer technique, which also provide gradient estimation for the velocity field (Dunlop et al. 2002). Figures 4(d)–(i) plot the pressure components, pressure anisotropy $A_{\text{gyr}} = P_\parallel/P_\perp$, and $P_i - D$ for ions and electrons, respectively. It can be seen that the ion pressure shows variations in both parallel and perpendicular directions, whereas the electron pressure is mostly varying in the parallel direction. Despite the larger pressures of ions compared with electrons, $P_i - D^{(e)}$ is larger than $P_i - D^{(i)}$ for nearly one order of magnitude. In addition, $P_i - D^{(e)}$ exhibits multiscale variations where it not only contains variations of similar scale and amplitude as its ion counterpart, but also comprises many sub-ion scale structures with higher amplitude. These results indicate a stronger and more complex pressure-strain interaction accompanied by the electron flow-induced strains. Furthermore, If we compare the trend between $-\Pi_{ij}D_{ij}$ and A_{gyr}, it can be found that $P_i - D^{(i)}$ changes almost simultaneously in phase with $A_{\text{gyr}}^{(i)}$ (Figures 4(e)–(f)), whereas $P_i - D^{(e)}$ changes in the anti-phase with $A_{\text{gyr}}^{(e)}$ (Figures 4(h)–(i)). Although the causal relation is not necessarily implied, the correlations may reflect an inherent link between the time series of the work done by the pressure-stress interaction and the pressure anisotropy. Specifically, the correlation between $P_i - D^{(i)}$ and $A_{\text{gyr}}^{(i)}$ found here seems to agree with the scenario proposed by Del Sarto & Pegoraro (2018), but the correlation for $P_i - D^{(e)}$ and $A_{\text{gyr}}^{(e)}$ still requires future theoretical explorations.

5. Conclusions and Discussion

In conclusion, we have analyzed for the first time plasma properties within an Alfvén vortex embedded in the Earth's turbulent magnetosheath. This in situ observation has been made possible, attributing to the high temporal particle measurements from the MMS mission. As illustrated in Figure 4(a), the Alfvén vortex has a radius around 10 proton gyroradius and is identified as a 2D quasi-monopole type. The magnetic field and velocity field are rotating along the vortex axis, mostly in the azimuthal directions. Within the vortex, both ions and electrons exhibit distinctive characteristics that separate from the ambient plasma.

1. The ion temperature displays variations within the vortex, which are correlated with the parallel current density. It reaches local maximum in the vortex center, then decreases and arrives to its local minimum within the inversed current before finally increasing again in the vortex edge. Electrons behave in an opposite way as compared with ions, where temperature variations are correlated with the parallel vorticity. It reaches local maximum near the vortex edge and the inversed current, while having the local minimum in the vortex center.

2. Ions are parallel anisotropic $T_\parallel > T_\perp$ within the $j_\parallel > 0$ regions and perpendicular anisotropic $T_\perp > T_\parallel$ within the $j_\parallel < 0$ regions. Electrons, on the contrary, are isotropic within the $j_\parallel > 0$ regions and parallel anisotropic $T_\parallel > T_\perp$ within the $j_\parallel < 0$ regions. The temperature anisotropies

for both components are correlated well with parallel current density/vorticity (see Figures 4(b) and (c)). The strongest ion anisotropy (i.e., $T_\parallel/T_\perp = 0.7$ and 1.4) occurs in the strong shear regions where the gradient of the field reaches maxima ($j_\parallel \sim \pm 200 \, \text{nA/m}^2$), but the strongest electron anisotropy ($T_\parallel/T_\perp = 2.5$) only occurs at local minimum of $j_\parallel \sim -200 \, \text{nA/m}^2$. The isotropic states of ions happen at crossings of the zero current (zero of the Bessel functions in the vortex solutions), while the isotropy of electrons happens at local maximum of $j_\parallel \sim 200 \, \text{nA/m}^2$.

3. Deformations of the VDFs, featuring elongations along or across the magnetic field, are modulated by $|\nabla v_\perp|$ and $|\nabla b_\perp|$. In particular, ion beams with positive parallel drifting speed (marked as ① in Figure 4(a)), together with bidirectional parallel electron beams (marked as ② in Figure 4(a)), are found within the vortex.

These results provide observational evidence of local kinetic processes within the Alfvén vortex, which may help to understand the intermittent heating and energy transfer processes within the coherent structures. In addition, the nonthermal temperature anisotropies and the deformations of ion and electron VDFs might introduce instabilities to the system (i.e., the cyclotron type when $T_\perp > T_\parallel$, or the firehose type when $T_\parallel/T_\perp$), which may in turn affect the small-scale turbulence cascade. Though only one event of a well-defined Alfvén vortex is presented in this Letter, a statistical study is being performed to further investigate the relation between Alfvén vortices and plasma kinetic effects in different scenarios.

One limitation of the current work is the interpretation of the fluctuations as described by the classical shear Alfvén vortex model, which is a solution of the Kadomtsev–Pogutse–Strauss system of the reduced incompressible MHD equations (Petviashvili & Pokhotelov 1992). This model only considers the nonlinear effects of the shear Alfvén waves, while the compressible effects have been neglected. Nevertheless, we note that the Alfvén vortex observed here, being similar with Alfvén vortices in the slow solar wind (Perrone et al. 2016), is in fact compressible. To describe the compressive coherent magnetic vortices in high-beta plasma, Jovanovic et al. (2017) has developed a new model. By omitting the heat flux and thus considering the equations of state, the normalized density fluctuations $\delta\hat{n} = \delta n/n_0$ and compressible magnetic field fluctuations $\delta\hat{B}_\parallel = \delta B_\parallel/B_0$ are solved via the generalized pressure balance condition. For the solutions at scales larger than ion Larmor radius, $\delta\hat{n}$ and $\delta\hat{B}_\parallel$ are localized within the vortex core. Their relative ratio, also known as plasma compressibility (Gary 1986), is expressed as

$$C_{\text{plasmas}} = \frac{\delta\hat{n}}{\delta\hat{B}_\parallel}$$

$$= \frac{\frac{\beta_{i\perp}}{4} + \frac{V_A^2}{u_z^2}\left(1 - \frac{\beta_{e\parallel} - \beta_{e\perp}}{2}\right)}{\frac{\beta_{i\perp}}{4} - \frac{V_A^2}{u_z^2}\frac{\gamma_{i\perp}\beta_{i\perp} + \gamma_{e\perp}\beta_{e\perp}}{2}\left(1 - \frac{\beta_{e\parallel} - \beta_{e\perp}}{2}\right)}. \quad (5)$$

Where u_z is the vortex speed along the magnetic field, and $\gamma_{i\perp}$ and $\gamma_{e\perp}$ are the polytropic indices for the ions and electrons, satisfying $T_{s,\perp} \propto n_s^{\gamma_\perp - 1}$. In comparison with this model, we find the following. (1) $\delta B_\parallel$ are localized within the vortex, while $\delta B_\perp$

"leaks out" from the core to larger distances (Figure 2(a)). The localization of $\delta B_\parallel$ is associated with the 3 s scale of the mean field, while the variations in $B_{\rm abs}$ (Figure 1) cover a wider range. (2) The observed $C_{\rm plasmas}$ (for the timescales from 0.3 to 3 s) could reach ~ 2 in the vortex core ($\delta n/n_0 \sim 0.32$, $\delta B_\parallel/B_0 \sim 0.15$), while the theoretical mean value estimated from Equation (5) is around 4, if we take $u_z/V_A = u_\perp/\tan(\theta_{\rm vortex})/V_A \sim 1.7$, $\beta_{i\perp} = 0.9$, $\beta_{e\parallel} = 0.18$, $\beta_{e\perp} = 0.1$, and use $\gamma_{i\perp} = 0.58 \pm 0.13$, $\gamma_{e\perp} = 1.1 \pm 0.04$ as fitted from the density and temperature measurement. Hence, the observed compressible features qualitatively agree with the theory of Jovanovic et al. (2017). It should be noted that $C_{\rm plasma}$ appears to be a sensitive function of $\theta_{\rm vortex}$. For example, if $\theta_{\rm vortex}$ is larger than 8°, $\delta B_\parallel/B_0$ may touch zero and $C_{\rm plasma}$ becomes infinite in our case, while if $\theta_{\rm vortex}$ is zero, u_z is infinite and $C_{\rm plasma}$ is 1. We also remark that the double polytropic equations, although lacking the kinetic features, may serve as a specific description for the thermal anisotropies of coherent structure (e.g., the interpretation of magnetic holes in Zhang et al. 2018). Future attempts on basis of polytropic laws need to be made to address the compressibility and thermal dynamics within the Alfvén vortex.

ORCID iDs

Tieyan Wang ⬤ https://orcid.org/0000-0003-3072-6139
Denise Perrone ⬤ https://orcid.org/0000-0003-1059-4853
Yu. V. Khotyaintsev ⬤ https://orcid.org/0000-0001-5550-3113
C. T. Russell ⬤ https://orcid.org/0000-0003-1639-8298

References

Alexandrova, O. 2008, NPGeo, 15, 95
Alexandrova, O., Chen, C. H. K., Sorriso-Valvo, L., Horbury, T. S., & Bale, S. D. 2013, SSRv, 178, 101
Alexandrova, O., Mangeney, A., Maksimovic, M., et al. 2004, JGRA, 109, A05207
Alexandrova, O., Mangeney, A., Maksimovic, M., et al. 2006, JGRA, 111, A12208
Alexandrova, O., & Saur, J. 2008, GeoRL, 35, L15102
Ashurst, W. T., Kerstein, A. R., Kerr, R. M., & Gibson, C. H. 1987, PhFl, 30, 2343
Biskamp, D. 2003, Magnetohydrodynamic Turbulence (Cambridge: Cambridge Univ. Press)
Burch, J. L., Moore, T. E., Torbert, R. B., & Giles, B. L. 2016, SSRv, 199, 5
Burlaga, L. F. 1990, JGR, 95, 4333
Camporeale, E., Sorriso-Valvo, L., Califano, F., & Retinò, A. 2018, PhRvL, 120, 125101
Cerri, S. S., Henri, P., Califano, F., et al. 2013, PhPl, 20, 112112
Chang, T. 1999, PhPl, 6, 4137
Chasapis, A., Retinò, A., Sahraoui, F., et al. 2015, ApJL, 804, L1

Chasapis, A., Yang, Y., Matthaeus, W. H., et al. 2018, ApJ, 862, 32
Chen, C. H. K. 2016, JPlPh, 82, 535820602
Chmyrev, V. M., Bilichenko, S. V., Pokhotelov, O. A., et al. 1988, PhyS, 38, 841
Del Sarto, D., & Pegoraro, F. 2018, MNRAS, 475, 181
Del Sarto, D., Pegoraro, F., & Califano, F. 2016, PhRvE, 93, 053203
Dong, X.-C., Dunlop, M. W., Wang, T.-Y., et al. 2018, JGRA, 123, 5464
Dunlop, M. W., Balogh, A., Glassmeier, K.-H., & Robert, P. 2002, JGRA, 107, 1384
Ergun, R. E., Tucker, S., Westfall, J., et al. 2016, SSRv, 199, 167
Escoubet, C. P., Fehringer, M., & Goldstein, M. 2001, AnGeo, 19, 1197
Farge, M. 1992, AnRFM, 24, 395
Franci, L., Hellinger, P., Matteini, L., Verdini, A., & Landi, S. 2016, in AIP Conf. Ser. 1720, SOLAR WIND 14: Proc. Fourteenth Int. Solar Wind Conf. 1720, ed. L. Wang et al. (Melville, NY: AIP), 040003
Frisch, U. 1995, Turbulence. The Legacy of A.N. Kolmogorov (Cambridge: Cambridge Univ. Press)
Gary, S. P. 1986, JPlPh, 35, 431
Greco, A., Chuychai, P., Matthaeus, W. H., Servidio, S., & Dmitruk, P. 2008, GeoRL, 35, L19111
Greco, A., Perri, S., Servidio, S., Yordanova, E., & Veltri, P. 2016, ApJL, 823, L39
Groselj, D., Chen, C. H. K., Mallet, A., et al. 2018, arXiv:1806.05741
Hasegawa, A., & Mima, K. 1978, PhFl, 21, 87
He, J., Tu, C., Marsch, E., et al. 2015a, ApJL, 813, L30
He, J., Tu, C., Marsch, E., & Yao, S. 2012, ApJL, 745, L8
He, J., Wang, L., Tu, C., Marsch, E., & Zong, Q. 2015b, ApJL, 800, L31
Horton, W., & Hasegawa, A. 1994, Chaos, 4, 227
Huang, S. Y., Sahraoui, F., Yuan, Z. G., et al. 2017, ApJL, 836, L27
Jovanovic, D., Alexandrova, O., Maksimovic, M., & Belic, M. 2017, arXiv:1705.02913
Karimabadi, H., Roytershteyn, V., Wan, M., et al. 2013, PhPl, 20, 012303
Kiyani, K. H., Osman, K. T., & Chapman, S. C. 2015, RSPTA, 373, 20140155
Lacombe, C., Alexandrova, O., Matteini, L., et al. 2014, ApJ, 796, 5
Lion, S., Alexandrova, O., & Zaslavsky, A. 2016, ApJ, 824, 47
Marsch, E., Schwenn, R., Rosenbauer, H., et al. 1982, JGR, 87, 52
Osman, K. T., Matthaeus, W. H., Hnat, B., & Chapman, S. C. 2012a, PhRvL, 108, 261103
Osman, K. T., Matthaeus, W. H., Wan, M., & Rappazzo, A. F. 2012b, PhRvL, 108, 261102
Parashar, T. N., & Matthaeus, W. H. 2016, ApJ, 832, 57
Parashar, T. N., Shay, M. A., Cassak, P. A., & Matthaeus, W. H. 2009, PhPl, 16, 032310
Perrone, D., Alexandrova, O., Mangeney, A., et al. 2016, ApJ, 826, 196
Perrone, D., Alexandrova, O., Roberts, O. W., et al. 2017, ApJ, 849, 49
Perrone, D., Valentini, F., Servidio, S., Dalena, S., & Veltri, P. 2013, ApJ, 762, 99
Perrone, D., Valentini, F., Servidio, S., & Veltri, P. 2014, EPJD, 68, 209
Petviashvili, V., & Pokhotelov, O. 1992, Solitary Waves in Plasmas and in the Atmosphere (London: Gordon and Breach)
Pezzi, O., Valentini, F., & Veltri, P. 2016, PhRvL, 116, 145001
Pollock, C., Moore, T., Jacques, A., et al. 2016, SSRv, 199, 331
Retinò, A., Sundkvist, D., Vaivads, A., et al. 2007, NatPh, 3, 236
Roberts, O. W., Li, X., Alexandrova, O., & Li, B. 2016, JGRA, 121, 3870
Russell, C. T., Anderson, B. J., Baumjohann, W., et al. 2016, SSRv, 199, 189
Schwartz, S. J. 1998, ISSIR, 1, 249
Servidio, S., Valentini, F., Califano, F., & Veltri, P. 2012, PhRvL, 108, 045001
Servidio, S., Valentini, F., Perrone, D., et al. 2015, JPlPh, 81, 325810107
She, Z.-S., Jackson, E., & Orszag, S. A. 1990, Natur, 344, 226
Shukla, P. K., Yu, M. Y., & Varma, R. K. 1985, PhFl, 28, 1719
Sorriso-Valvo, L., Carbone, V., Giuliani, P., et al. 2001, P&SS, 49, 1193
Stasiewicz, K., Bellan, P., Chaston, C., et al. 2000, SSRv, 92, 423
Sundkvist, D., Krasnoselskikh, V., Shukla, P. K., et al. 2005, Natur, 436, 825
Torbert, R. B., Russell, C. T., Magnes, W., et al. 2016, SSRv, 199, 105
Torrence, C., & Compo, G. P. 1998, BAMS, 79, 61
Tu, C.-Y., & Marsch, E. 1995, SSRv, 73, 1
Valentini, F., Perrone, D., Stabile, S., et al. 2016, NJPh, 18, 125001
Valentini, F., Perrone, D., & Veltri, P. 2011, ApJ, 739, 54
Veltri, P., & Mangeney, A. 1999, in AIP Conf. Ser. 471, Solar Wind IX, ed. S. R. Habbal et al. (Melville, NY: AIP), 543
Vianello, N., Spolaore, M., Martines, E., et al. 2010, NucFu, 50, 042002
Volwerk, M., Louarn, P., Chust, T., et al. 1996, JGR, 101, 13335
Vörös, Z., Yordanova, E., Varsani, A., et al. 2017, JGRA, 122, 11

Wan, M., Matthaeus, W. H., Karimabadi, H., et al. 2012, PhRvL, 109, 195001

Wang, T., Cao, J.-B., Fu, H., Liu, W., & Dunlop, M. 2014, JGRA, 119, 9527

Wang, X., He, J., Tu, C., et al. 2012, ApJ, 746, 147

Wang, X., Tu, C., He, J., Marsch, E., & Wang, L. 2013, ApJL, 772, L14

Wu, P., Perri, S., Osman, K., et al. 2013, ApJL, 763, L30

Yang, Y., Matthaeus, W. H., Parashar, T. N., et al. 2017a, PhRvE, 95, 061201

Yang, Y., Matthaeus, W. H., Parashar, T. N., et al. 2017b, PhPl, 24, 072306

Yordanova, E., Vörös, Z., Varsani, A., et al. 2016, GeoRL, 43, 5969

Zank, G. P., Adhikari, L., Hunana, P., et al. 2017, ApJ, 835, 147

Zhang, L., He, J., Tu, C., et al. 2015, ApJL, 804, L43

Zhang, L., He, J., Zhao, J., Yao, S., & Feng, X. 2018, ApJ, 864, 35

Zhao, J. S., Wang, T. Y., Dunlop, M. W., et al. 2018, ApJ, 867, 58

Zimbardo, G., Greco, A., Sorriso-Valvo, L., et al. 2010, SSRv, 156, 89